A Secondary Reaction Pathway for the Alumina Atomic Layer Deposition Process with Trimethylaluminum and Water, Revealed by Full-Range, Time-Resolved In Situ Mass Spectrometry

Reference

Andreas Werbrouck, Mahdi Shirazi, Felix Mattelaer, Simon D. Elliott, Jolien Dendooven, Christophe Detavernier
A Secondary Reaction Pathway for the Alumina Atomic Layer Deposition Process with Trimethylaluminum and Water, Revealed by Full-Range, Time-Resolved In Situ Mass Spectrometry
J. Phys. Chem. C 2020, 124, 48, 26443–26454
Publication Date: November 20, 2020
https://doi.org/10.1021/acs.jpcc.0c07602

A Secondary Reaction Pathway for the Alumina Atomic Layer Deposition Process with Trimethylaluminum and Water, Revealed by Full-Range, Time-Resolved In Situ Mass Spectrometry

Andreas Werbrouck,[†] Mahdi Shirazi,[‡] Felix Mattelaer,[†] Simon D. Elliott,[¶] Jolien Dendooven,[†] and Christophe Detavernier*[,†]

†*Department of Solid State Sciences, Ghent University, Krijgslaan 281, 9000 Ghent, Belgium*

‡*Department of Applied Physics, Eindhoven University of Technology, P. O. Box 513, 5600 MB, Eindhoven, The Netherlands*

¶*Schrödinger Inc., 120 West 45th Street, 17th Floor, New York, NY 10036-4041, USA*

E-mail: Christophe.Detavernier@ugent.be

Abstract

A method to obtain full mass-over-charge (m/z), time-resolved quadruple mass spectrometry (QMS) spectra of an atomic layer deposition (ALD) cycle is proposed. This method allows one to circumvent the limitations of traditional approaches for obtaining QMS information in ALD, as all m/z values can be simultaneously screened for the formation of reaction products in an efficient way. As a proof of concept this method was applied to the trimethylaluminum (TMA)-water process. This process has been studied extensively over the past decades. Besides the expected formation of CH_4, the formation of gaseous $HOAl(CH_3)_2$ during the water pulse is observed, revealing a secondary reaction pathway for the water. The reaction energy and Gibbs free energy for different reactions are investigated computationally using density functional theory calculations, and confirm that the secondary reaction pathway is thermodynamically allowed for certain surface conditions.

Introduction

Atomic layer deposition (ALD) is a deposition method in which several gases and molecular vapors (precursors) are pulsed in a cyclic way to deposit thin, uniform and conformal films. In an ideal ALD process, the gaseous precursor molecules can only react with the available surface groups. Because these reactions are self-limiting, films can be grown with excellent thickness control, (sub)monolayer by (sub)monolayer, even in complex 3D structures.[1] Over the past years a plethora of processes has been reported, and several reviews exist in which available chemistries and intricate ALD subtleties are treated extensively.[2–4]

The TMA-water ALD process

One archetypical ALD process is the combination of trimethylaluminum (TMA) as precursor A (metal source) and water as precursor B (oxygen source).[4,5] The reaction mechanism is often described in an simplified manner: as the TMA arrives at an OH-terminated sur-

face, its methyl ligands can react with surface hydrogen, releasing CH_4. The subsequent time-or space-separated water pulse then removes the remaining methyl groups, again releasing methane as a reaction product. Indeed there is substantial evidence that CH_4 is formed during both pulses, and 'ligand exchange' is the main growth mechanism. The cartoonesque depiction of ligand exchange in the TMA-water process is frequently encountered in introductory slides, and probably known to every ALD practitioner in the field.

However, over the past years, several reports were published, providing clues that this process may not be as simple as is sometimes presented. Already in the review of Puurunen it was mentioned that increasing the temperature reduces the number of hydroxyl groups at the surface, effectively lowering the number of reaction sites for TMA.[4] Shirazi and Elliott have explained the self-limiting nature of ALD in terms of a cooperative effect,[6] leading to a coverage-dependent activation energy. The presence of remaining adsorbates (TMA fragments) in the neighborhood of a CH_3 ligand facilitates proton transfer and ligand desorption, leading to an increase in coordination of both the surface Al and O. Guerra-Nuñez *et al.* have shown mechanistically that the hydrogen content in ALD-deposited Al_2O_3 originates from rehydroxylation of the O-Al bonds during the water pulse.[7] Vandalon *et al.* have observed persistent CH_3 groups on the surface during the water pulse, in particular at low substrate temperature. It was proposed that either two kinds of CH_3 sites were present, or that the reaction cross-section was coverage dependent. The latter argument was given as well by Sperling *et al.*, explaining the double exponential decay of surface CH_3 groups observed by *in situ* infrared spectroscopy during the water pulse.[8] This was solved tentatively by introducing a coverage-dependent activation energy. It seems that, after all, the TMA-water process is not as ideal as generally believed. Especially during the water pulse, temperature- and coverage-dependent effects have to be accounted for.

Quadrupole mass spectrometry (QMS)

To study ALD processes to the level of detail of the previously mentioned studies, *in situ* methodologies are indispensable. They essentially open up the black box of the ALD reactor and allow the practitioner to obtain invaluable insights into growth mechanisms, kinetics, surface chemistry and film properties during the process. Several techniques are available to the experimenter, such as spectroscopic ellipsometry,[9] quartz crystal microbalance,[10] infrared spectroscopy,[11] (quadrupole) mass spectrometry[12] and even synchrotron-based X-ray techniques,[13] all revealing different aspects of the growth and chemistry. Often, they have to be combined in order to gain a deeper level of understanding of chemical reactions happening at the substrate surface.[14] Quadrupole mass spectrometry, the technique used in this paper, yields a unique insight into the gas composition in the reactor, but proper acquisition and interpretation of mass spectra is not straightforward. With the increasing importance of understanding and developing so-called *atomic layer etching* and in general *atomic layer processing* techniques,[15] knowledge of the gas phase constituents will become ever more important.

Challenges for QMS in ALD research

QMS is a commonly used technique for molecule identification. It ionizes and fragments incoming molecules, and measures the mass-over-charge (m/z) ratio of these fragments. As usually the charge is 1, we will use mass-over-charge and mass interchangeably in the following. The quadrupole scanning and detection hardware can probe only a single mass at the same time. This allows for two general measurement modes: a measurement of a large number of masses within a certain range, with limited time resolution, or the probing of only a couple of masses with a decent time resolution.

In most cases, for example peptide chemistry, a limited time resolution is hardly a problem: a semi-infinite source of a single, relatively pure compound is available. This allows for long integration times to obtain good signal-to-noise ratios on the mass-to-charge spec-

trum. From the masses of the different fragments and their combinations, the structure and constituents of the molecule can then be inferred.[16] Infrared spectroscopy and NMR deliver complementary information, and dedicated software has been developed to assist in analyzing the mass spectrometry data.[17]

In ALD process characterization on the other hand, we face an inherently different use case: the precursor molecules involved in the reaction are known in advance, and rather abundant, but therefore usually not of interest during the *in situ* experiment. Opposite to that, the reaction products that we are interested in are very limited in quantity, since they stem from a self-limiting surface reaction forming a (sub)monolayer at the substrate and the reactor walls. This implies that not only the amount of reaction product(s) is very limited ($\approx 10^{14}$ atoms/cm^2),[12] they are also present in the reactor for only a fleeting moment in time. Being able to measure with a good time resolution thus becomes of critical importance. In the ideal case, this good time resolution should not be confined to only one or a few masses, since in order to identify a complex reaction product, one will typically need its full mass spectrum. To circumvent this, researchers have to guess in advance which by-products are created, relying on information from other experiments, modeling and chemical intuition. In any case, this is a non-trivial task, and there is always the possibility that a critical mass is overlooked.

Ideally, most of these issues would be solved if we could collect full m/z spectra with a decent time resolution. It would even be possible to derive reaction mechanisms from the mass spectra instead of merely confirming them. However, this proposition seems largely incompatible with the nature of the measurement device combined with the self-limiting, low-quantity reactions going on during ALD.[18] Some groups have addressed these problems by adopting a method whereby a couple of masses are measured every cycle, hence creating high time resolution mass spectra for a larger range of masses.[18–20] Here, we propose another elegant solution for this problem.

The organization of this paper is as follows: in a first part, we propose a dedicated

sampling scheme and post-processing methodology for the mass spectra. In a second part, we use the TMA-water process as an experimental case study for the technique. Apart from CH_4, a second reaction product was observed during the water pulse. It was identified as $HOAl(CH_3)_2$. The computational validation of this reaction product by DFT calculations is treated in the third part of the paper. In the discussion, we interpret these results in view of the available literature and lay out possible directions for future research.

Experimental Methods

ALD depositions

All data were collected on a home-built, cold-wall, vacuum-type ALD reactor with mass spectrometer in a differentially pumped system (Fig. S1). All mass spectrometry experiments were conducted with a Hiden HPR-30 mass spectrometer with two detectors, a Faraday cup, and a secondary electron multiplier (SEM). The SEM detector was used for all experiments. The tube (diameter 5 cm) connecting the mass spectrometer to the reactor was heated and had a controllable pneumatic valve (opening diameter 5 cm) so access to the mass spectrometer could be controlled by the ALD software. For the depositions on powder, around 1g Al_2O_3 powder (3μm diameter) was used. No powder was lost during the depositions. Before we studied processes with mass spectrometry, they were thoroughly characterized with in situ ellipsometry and XPS. We were able to reproduce growth per cycle, temperature characteristics and composition as reported in literature. TMA (Strem, 97%) and deionized water were used for the TMA-water process.

A continuous background was visible in the spectrum: some peaks were intrinsically more intense than others. If the chamber is pumped from atmosphere, we assume the remaining background to retain the same atmospheric composition, with additional water, desorbed from the walls. Some remnants of ambient atmosphere at masses 28, 32, 40, and 44 could be seen, and a signal at 69 originating either from a lubricant or oil from a pump,

or from so-called McLafferty rearrangement (recombination of organic molecules in a mass spectrometer).[21] Leak testing with ether was performed, without finding any leak. As none of these signals seem to change during the process, and clear signals from reaction products are observed, we assumed that these signals were not of importance to the measurements and subtracted them from the spectrum. Time-resolved spectra were smoothed on the time axis with a rolling average window of 10 data points.

Computational details

Density functional theory (DFT) was employed to calculate the reaction energies of the main products. The crystalline form of corundum or α-aluminium oxide has been considered, which is the most common crystalline phase of aluminium oxide. The slab of $Al_2O_3(0001)$ was generated by cleaving the optimized bulk structure of corundum. This has been done in such a way to gain the maximum number of O at the bottom and top surfaces of the slab. The Al atoms had the maximum coordination number (c.n.) of 6 (bulk-like Al). While the bare slab was oxygen-rich, adding H atoms to the bare O at the bottom and top of slab restored the stoichiometry and preserved the neutrality of the slab. Surfaces were separated by 10 Å of vacuum and the cell was expanded by 2×2×1. Hence, the final slab had 116 atoms ($Al_{32}O_{60}H_{24}$) with 480 electrons.

In thermal ALD, several cycles are often needed to deposit a mono-layer of a compound. The top surface is therefore generally not a closed smooth layer during ALD. To describe the consequence of different local chemistry (different OH-coverage) on the formation of by-products, various surface models were generated by randomly removing an OH group and a H-atom (as H_2O molecule) from the fully OH-covered $Al_2O_3(0001)$ top surface. It is known that many OH groups remain unreacted in the as-deposited thin film[7] and we therefore considered the removal of half of the surface OH (three H_2O molecules per slab). This generated a set of configurations with different OH-coverage for each reaction. Obviously, the sub-layers are fully crystalline and stoichiometric. The generated configurations were

fed into the ab initio calculator (VASP)[22] to calculate the reaction energies. The atomic simulation environment (ASE)[23] was employed to manage these calculations.

Further computational details can be found in the Supporting Information, section .

Results

Strategy towards capture of time-resolved mass spectra

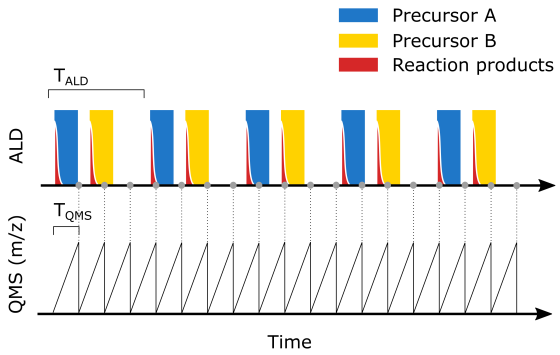

Figure 1: Schematic illustration of the data collection process. Note that all masses may be monitored several times each ALD cycle, and will be recorded at different times in different cycles.

To solve the incompatibility between the limited time resolution of the spectrometer and our desire to gather time-resolved spectra, we will exploit the fact that ALD processes are cyclical in nature. After the first cycles where initial growth effects could be of importance, the so-called steady state growth regime is reached. In this regime the chemistry of each subsequent ALD cycle should be identical. During the deposition, we collect full spectra with a poor time resolution. It is generally not possible to get any meaningful insight from data of only one ALD cycle. However, in view of the repetitive nature of the ALD process, the deposition cycle can be repeated as many times as necessary to gather a sufficient amount of data with a proper signal-to-noise ratio (Fig. 1). Since any proper mass spectrometry software will also save the exact time a particular datapoint or (in our case) spectrum is

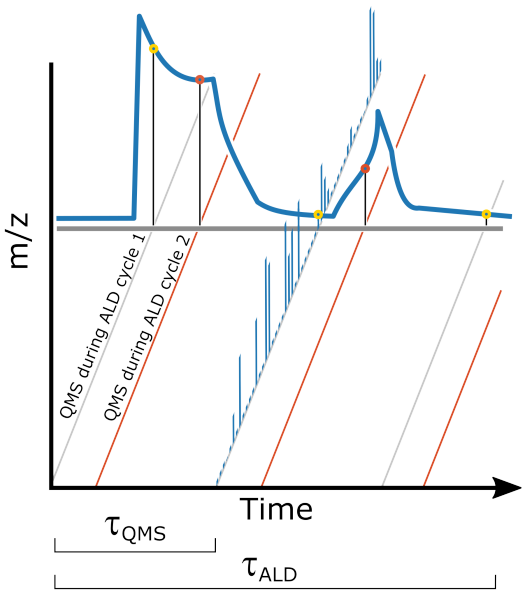

Figure 2: Schematic overview of how the linescan spectra populate the time-resolved spectrum, after taking the modulus of the time series. The true intensity profile for a given mass $I(m_i, t)$ is shown as a continuous blue line. This profile is sampled at different times in different ALD cycles. The QMS spectrum recorded during the first cycle (grey lines) are offset from the QMS recorded during the second (red lines) and so forth. Repeating this eventually leads to a satisfactory time resolution for every mass. The yellow and red dots show data for this particular m/z obtained in the first and second cycle, respectively.

collected, it is possible to interpolate the exact time each datapoint is measured. The result of the experiment is a time series of (up to millions of) data points, combining a time in the process with a mass-over-charge ratio and a partial pressure. Considering the exact time of each data point, one can envision calculating the modulo of this time with the length of one ALD cycle, which allows us to compress the extended time series into a time-resolved mass spectrum of a single ALD cycle (Fig. 2).

To formalize this, consider an ALD process with two precursors, A and B, and period τ_{ALD} (the time necessary for a single process cycle). In the beginning of each precursor pulse, a certain fraction of the precursor molecules will react with the surface groups and form reaction products. The underlying, fundamental mass spectrum of this ALD process can be denoted as $I(m/z, t)$, such that

$$I(m/z, t) = I(m/z, t + k \cdot \tau_{\text{ALD}}) \tag{1}$$

for all integer k's. The mass spectrometer can evaluate this underlying function, but only one m/z at a time in a range of masses 1 to M and with integration time $t_{\text{integration}}$, such that we get a series

$$\begin{aligned} &I_{\text{QMS},1}(m_1, t_1), \\ &I_{\text{QMS},2}(m_2, t_2), \\ &I_{\text{QMS},3}(m_3, t_3), \\ &... \end{aligned} \tag{2}$$

with $t_{n+1} = t_n + t_{\text{integration}}$, $M \cdot t_{\text{integration}} = \tau_{\text{QMS}}$ and m_i denoting a specific m/z. If the ALD process has K cycles, the QMS can measure L spectra in the meantime, with

$$L = K \cdot \frac{\tau_{\text{ALD}}}{\tau_{\text{QMS}}} \tag{3}$$

After the process, we consider the time series for one specific m/z: m_i. We have collected L sampling points

$$\begin{aligned} &I(m_i, t_0), \\ &I(m_i, t_0 + \tau_{\text{QMS}}), \\ &..., \\ &I(m_i, t_0 + (L-1) \cdot \tau_{\text{QMS}}) \end{aligned} \tag{4}$$

Because the function $I(m/z, t)$ is periodic with period τ_{ALD} for each m_i, we can map this entire series to the range $[0, \tau_{\text{ALD}}]$ by computing

$$I\left(m_i, (t_0 + l \cdot \tau_{\mathrm{QMS}}) \bmod \tau_{\mathrm{ALD}}\right) \tag{5}$$

with $0 \leq l \leq L-1$ and reordering the series so we obtain $I(m_i, t_j)$ with

$$0 < (t_0 + l \cdot \tau_{\mathrm{QMS}}) \bmod \tau_{\mathrm{ALD}} = t_j \leq \tau_{\mathrm{ALD}} \tag{6}$$

This allows to reconstruct the true $I(m/z, t)$ for one ALD cycle with period τ_{ALD}, without the constraints imposed by the mass spectrometer. The time resolution Δt between different points depends on $\frac{\tau_{\mathrm{QMS}}}{\tau_{\mathrm{ALD}}}$. Calculations on how this can be optimized can be found in the Supporting Information. Where Sperling *et al.* relied on hardware triggers to synchronize and average out their IR measurements, we solely rely on post-processing the data to construct the time-resolved spectrum.[24,25]

Practical issues

When naively applying the scheme depicted in Fig. 2, it became apparent that it is critical to determine the exact value of τ_{ALD}, because the slightest error on the length of the ALD cycle will increase the misalignment of subsequent cycles in the post-processing. In the in-house developed software used to control our ALD reactor, it is possible to schedule actions with 1 s resolution. The execution of the commands is performed in loops with a time-out period of 100 ms. So a 30-cycle deposition in which 5 actions are performed each cycle, each action with 20 ms delay, would lead to a misalignment of the data collected in the last cycle of about 2.9 s. This is way too much if we expect exact time placement of the data. For day-to-day depositions this moderate deviation on the expected cycle time is not an issue, but since we need the length of the cycle with high precision, this error becomes important when constructing the time-resolved m/z spectrum. However, the error on this cycle length is systematic, so it is possible to determine the cycle time with a higher resolution. For the sake of notation: where we assumed before that $\tau_{\mathrm{ALD}} = \tau_{process}$, now this is further specified

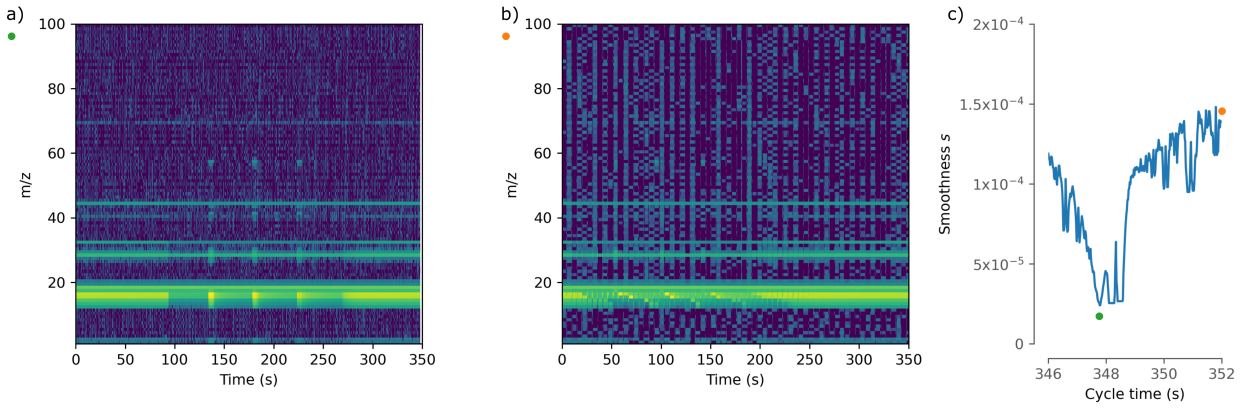

Figure 3: Determining the exact cycle time is paramount to get proper measurements. a) time-resolved spectrum of 3 water pulses with proper determination of τ_{error} where s is minimal. The full time range is shown, also showing the part where the valve to the chamber is closed. b) time-resolved spectrum with suboptimal τ_{error}. The data is very noisy, sudden jumps appear, increasing the amount of noise. c) Smoothness function given by eq. 7 for various τ_{ALD}. If every point is in its optimal position, the noise will be mimimal (green circle). The W-shaped features right of the minimum sometimes appear due to nonideal sampling. An animation showing different $I_{\tau_{\text{ALD}}}$ with the smoothness function is provided in supporting information.

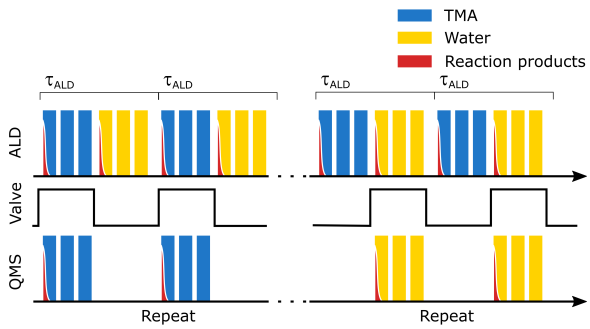

Figure 4: Pulsing scheme used for the TMA-H_2O measurements. It is clear that the mass spectrometer sees only a single TMA-water cycle. The valve is installed between the spectrometer and the reactor (see Fig. S1)

as $\tau_{\text{ALD}} = \tau_{process} + \tau_{error}$.

After some initial attempts of determining τ_{error} by hand, a more systematic solution was explored. Minimizing the noise in the final data matrix seemed to give the best results: we recalculate the data matrix for different τ_{ALD} and for every matrix $I_{\tau_{\text{ALD}}}$ we calculate the smoothness s with

$$s = \sum_{i=0}^{M} \sum_{j=0}^{L} |I_{\tau_{\mathrm{ALD}}}(m_i, t_j) - I_{\tau_{\mathrm{ALD}}}(m_i, t_{j+1})| \tag{7}$$

on the data matrix. Doing this for a number of cycle times we usually find a clear minimum (see Fig. 3, video and scripts in the supporting information). This methodology can be justified by considering that since the partial pressures are identical in each cycle, the evolution of the partial pressure for a certain mass over charge ratio should be as smooth as possible.

To obtain the best possible visualization, the data can be somewhat smoothed after determining the cycle length, and if necessary clipped. For clipping the lower threshold should be taken so all relevant peaks are still visible, while the upper threshold should seek to show as much differences in partial pressure while giving the best possible contrast. For example when argon is used as a carrier gas, the intensity of the m/z = 40 and m/z = 20 (double ionization) peaks might be orders of magnitude higher than the intensity of reaction products. It might be convenient to clip these values to a somewhat lower threshold, even when log scales are used for the intensity scale.

A final warning might apply. As most people familiar with the nature of ALD will be aware of, the technique is able to very efficiently coat every surface within reach of the gas. Even though the pressure in the mass spectrometer is orders of magnitude lower than the pressure in the reactor, eventually the interior of the spectrometer may get coated. This can be solved elegantly by heating the spectrometer walls to avoid condensation, and, most importantly, by controlling access to the mass spectrometer and probing only one half-reaction at a time. For TMA-water, this is critical, as discussed below. In general, with a pulsing scheme as n times (AAA)BBB followed by n times AAA(BBB). The brackets indicate when the valve to the mass spectrometer (see Fig. S1) is open and one is able to collect data. As can be seen in Fig. 4, this results in only a single AB ALD cycle in the spectrometer itself.

Species identification

Given the time-resolved spectrum, identification of the peaks may be another challenging task. Here the 'fingerprint' of the molecule comes into play: given a single parent molecular species in the reactor, the intensity ratio for different m/z peaks should remain constant. A good start is often to try to identify the precursors and/or their fragments, although it is possible that no signal for the full molecule is observed if its ion is unstable. If this is considered a problem, lower electron energies can be applied to prevent further fragmentation, but as this changes peak intensities, a part of the 'fingerprint' information is lost. The reaction products formed during ALD may be very similar to a ligand (L) of the precursor, especially if it is in the HL form. E.g. the spectrum from methane (CH_4, m/z = 16) generated in the TMA-water process may get mixed up in the spectrum of TMA, where methyl (m/z = 15) is very prominent). To separate those contributions, dedicated pulsing schemes are commonly employed although sometimes a simple measurement during a an AB-cycle may as well be convincing. The AAA(ABABAB)BBB sequence is commonly employed in literature, following the standard set by the Helsinki group,[12] where Hyvärinen used a slightly different ABABAB(AAA)ABABAB scheme. We will further adapt this pulsing scheme, by repeating an AAABBB cycle. This way, we create an internal reference for our measurements. Lu *et al.* used a similar scheme.[26] Identification of reaction products can then happen in a top-down way, proposing molecules for the signals with highest m/z and matching spectra with (protonated) fragments. This protonation in the mass spectrometer is a known phenomenon[12] and the main driver for the use of D_2O instead of water as a reactant.

A case study for TMA-water

As a proof of principle, the TMA-H_2O process is studied on an Al_2O_3 powder, at a temperature of 150°C (Fig. 5). The pulsing sequence is indicated in Fig. 4. It is generally accepted that when the TMA molecule reaches an OH-terminated surface, the following reaction takes place

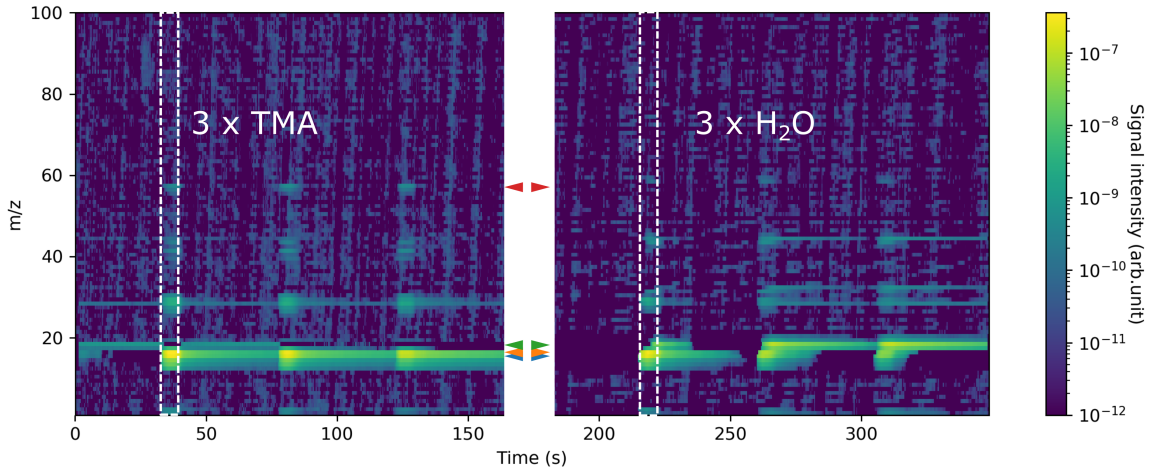

Figure 5: Time-resolved mass spectra probing the underlying chemistry for the TMA-water process. Vertical slices are integrated over the region indicated by the white dashed boxes and shown in Fig. 6. Horizontal slices are indicated by the coloured arrows in the middle and are shown in Fig. 7, compared with classical MID measurements. The spectrum for the TMA pulse without background subtraction can be seen in Fig. 3. The spectrum for water has a very similar background.

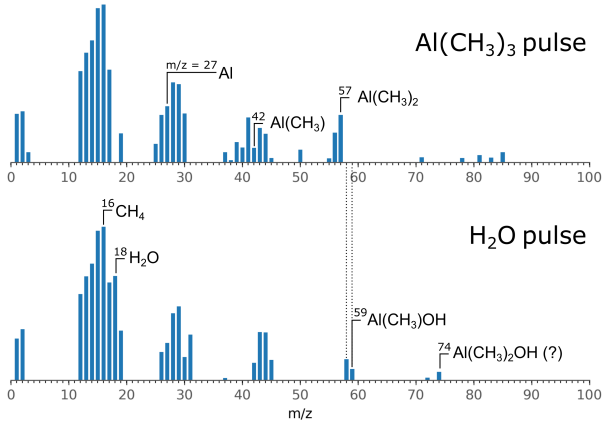

Figure 6: Integrated data (log scale) for the boxes shown in Fig. 5. From the subtle differences at m/z=59 we can infer that the parent molecule is different. Even at m/z = 74 we see a slight hint, but it is not conclusive. In Fig. 8 the water pulse chemistry is probed with higher sensitivity and the existence of a parent molecule at m/z 74 is confirmed.

$$\mathrm{xOH(s) + Al(CH_3)_3(g) \longrightarrow O_xAl(CH_3)_{3\text{-}x}(s) + xCH_4(g)}$$

Followed by

$$O_xAl(CH_3)_{3-x}(s) + (3-x)H_2O(g) \longrightarrow AlO_3H_x(s) + (3-x)CH_4(g)$$

when water is pulsed (with x 1 or 2). Note that in the final structure, the O atoms of the Al_2O_3 will be shared between Al atoms, leading to the Al_2O_3 stoichiometry. Methane (CH_4, m/z=16) should be the only gaseous reaction product involved in this process. Reactions considered for the computational study are shown in Table 1. The spectrum of TMA (Fig. 6) exhibits peaks at m/z 72 ($Al(CH_3)_3$) , 57 ($Al(CH_3)_2$), 42 ($AlCH_3$), 27 (Al) and 15 (CH_3) with some spread due to additional H loss or capture. The third pulse of TMA in Fig. 5 serves here as a reference, as for this pulse all self-limiting reactions are assumed to have been completed, so only the precursor-originated mass fragments can be detected. Surrounding mass over charge ratios may also be higher in intensity since the loss or gain of a hydrogen atom will change the mass of the fragment. Water will exhibit peaks at 18, 17 (OH, far less intense) 19 (due to deuterium) and 16 (O, also not intense). We will measure also for almost every precursor peaks at m/z 1 and 2 (and quite a strong background as well) stemming from hydrogen fragments, which are difficult to pump away with a turbo pump. Three pulses of TMA (5 seconds, 40 seconds wait time) were followed by three pulses of H_2O (5 seconds, 40 seconds wait time) with 40 seconds after every opening/closing of the valve to the mass spectrometer to allow the spectrometer interior to equilibrate with the reactor. This was repeated 60 cycles, where the first 30 cycles the TMA pulse was probed, and the following 30 cycles the water pulse was probed. After 8 cycles we considered initial effects vanished, so for the TMA characterization, we only used 22 cycles. The time resolution (distance between points of the same mass) of this measurement is an oscillating function with average value $\Delta t = \overline{t_{j+1} - t_j} = 0.236 \pm 0.159$ s and $\Delta t_{\max} = 0.519s$. The integration time is 0.045 s, by averaging out we can increase the signal-to-noise ratio. In the Supporting Information, more information on the time resolution of these time-resolved measurements is provided. The time resolution of a classical multiple ion detection (MID) measurement is dependent on integration time and number of ions followed, while the number of averaged-out cycles determines the signal-to-noise-ratio.

While all data can be plotted as if they were detected in multiple-ion mode (a single line per m/z) we found it more convenient to plot the three-dimensional data given by $I(m/z, t)$ with a heat map to get an overview of the full cycle chemistry (Fig. 5). Integration over a specific timeframe allows one to see the full spectrum of the gas mix in the reactor at a particular time (Fig. 6 and taking slices allows to study the time evolution of certain masses (Fig. 7)).

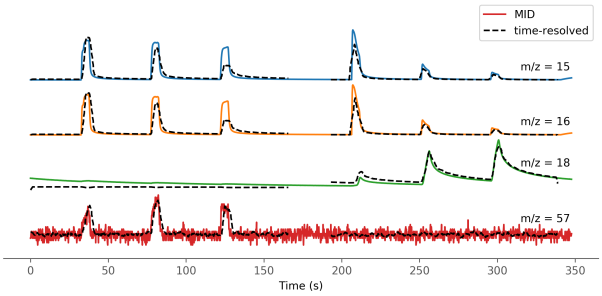

Figure 7: Comparison of MID data with slices of the time-resolved spectrum.

Measurement validation

Immediately after collecting data for the construction of a time-resolved spectrum (Fig. 5), a measurement was performed in the traditional MID mode, where only m/z 15, 16, 18 and 57 were followed. Three cycles of the identical process were performed and averaged out. The valve to the mass spectrometer was opened all the time. When the data are compared in Fig. 7, it can be seen that the time-resolved data reasonably agree with the MID data. The water intensity rises over time in the ALD cycle, together with a drop in intensity for methane (m/z = 16 and 15), indicating saturation at the surface. Main differences are the more pronounced decrease of the methane signal in the time-resolved mode during the TMA pulse while the MID signal stays relatively constant. We have no explanation for this discrepancy. Another difference is the reduction of the background signal (for example in the m/z = 18 spectrum) caused by the valve. This suggests that there is some contribution to the signal from background in the mass spectrometer.

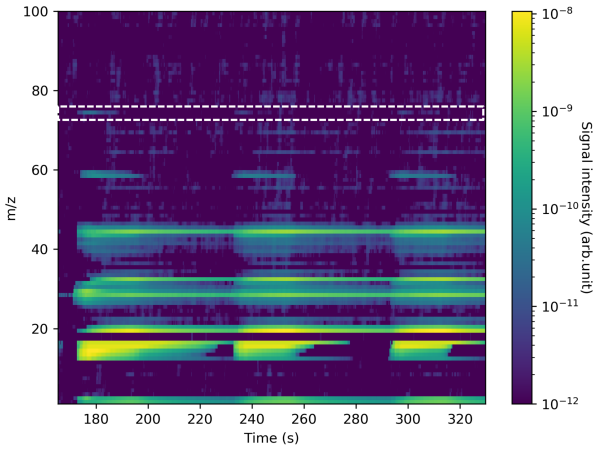

Figure 8: Three water pulses in TMA-water process, measured with higher resolution (than in Fig. 5). As expected from the earlier experiment, a transient peak emerges at m/z = 74 (white box), confirming the release of $HOAl(CH_3)_2$. Note that the water intensity constantly saturated the detector, so the background subtraction algorithm just subtracted the entire signal.

Assessing the quality of the measurements, the time-resolved signal is more representative of the steady-state condition as it comprises data from more cycles, where an MID measurement might be sensitive to time-dependent effects such as a different precursor pressure over time, heating effects or initial growth effects.

Secondary reaction products

The time-resolved spectra in Fig. 5 reveal that other reactions occur during the H_2O pulse, besides the formation of CH_4. We see peaks at m/z 59, 58 and below (Fig. 6), while we expected no fragments with a mass above m/z = 18. This suggests that a TMA-like molecule might be released during the water process. The observed mass to charge ratios point towards the release of $HOAl(CH_3)_2$ molecules during the water pulse.

The generation of $HOAl(CH_3)_2$ should also lead to a signal at m/z = 74. This mass is not convincingly observed in Fig. 5 (right side) and only a hint is present in Fig. 6. A new measurement was performed with higher integration time (65 ms instead of 45 ms), and higher sensitivity. The signals of water at m/z=18 are now clipped, but detection of

lower-intensity signals is favored. The signal at m/z = 74 can now clearly be distinguished (in Fig. 8). $HOAl(CH_3)_2$ might be a previously unnoticed, but important secondary reaction product during the TMA-water process.

Besides, it should be noted that during the TMA pulse, no signal pointing towards the release of $HOAl(CH_3)_2$ is given. There is however a transient signal at m/z = 29 (Fig. S4). This could be due to an AlH_2 or C_2H_5 ion, possibly due to a methane dimer. The similar shape of the peaks and the shape of other Al-containing peaks seem to hint towards the latter interpretation (see supplementary info). As no transient peaks are observed at other masses, we will not focus further on this mass.

Merits and limitations of time-resolved full-range mass spectrometry

To accurately assess the merits and limitations of our method, different aspects of time resolution, sensitivity, and accuracy should be considered.

A first important indicator is the time resolution of the spectrum (i.e. the Δt in between datapoints for the same m/z). One of the main advantages of the method is that the time resolution of full-range spectra is increased. MID measurements might offer a more straightforward way to measure peak shapes, if better time resolution is necessary. As noted before, the time resolution of the final time-resolved spectrum oscillates depending on the ratio $\frac{\tau_{\mathrm{QMS}}}{\tau_{\mathrm{ALD}}}$ (see supporting information for an extensive discussion on the time resolution). The number of cycles that are combined in the time-resolved, single cycle graph can be increased arbitrarily, as long as the error on the cycle time remains the same. This is dependent on the computer. We have run processes for more than 10h without synchronization issues. In this respect, it is noteworthy to mention that the high time resolution of MID measurements may be even unnecessary high: the pump-type design of the reactor works in our advantage, as the reactions go relatively slow because of the low pressure.

A second criterion to consider is the accuracy of the measurement. That means, is the measurement reliable, and representative of steady-state conditions. Either in the ALD

process or in the mass spectrometer, fluctuations and transients can influence the measurement. In that regard, MID measurements are prone to errors, especially if one manually has to change the settings in between measurements. Averaging out over several cycles might help here, but even then our method averages over *all* measured cycles, albeit probably with a worse time resolution. As all masses are measured at the same time, the correlation along the m/z axis is greater and one can be sure that the measurements reflect the steady-state $I(m/z, t)$ of this particular pulsing sequence. The lack of signal at some masses may strengthen the significance of detected signals at other masses. A signal that varies over the process can be observed with our method when $I(m/z, t)$ is plotted as-measured, without the data reorganization. It is necessary that the reorganization is carried out when the process is in steady-state.

One challenge with our method might be the determination of the minimum of the smoothness function s. This may become less obvious if pressure profiles lack a clear evolution, if the number of datapoints is limited, or if only a couple of masses give rise to peaks and a large m/z range is measured. This means that scanning larger ranges to probe molecules with larger masses (giving rise to more peaks) is feasible, as long as the quadrupole range is not the limiting factor.

Regarding to the sensitivity and dynamic range of the spectrometer there is less difference between different approaches. Typically a dynamic range has to be specified for the detector. Given sufficient integration time, it is possible to measure extremely low pressures. However, if the partial pressure of the fragment of interest is below the noise level of the dynamic range used, it is nearly impossible to measure in a convincing way. With these settings, the detector quickly saturates for species with a higher partial pressure, as demonstrated in Fig. 8. The only solution then is try to increase the signal, for example by using a larger surface area substrate.

This being said, the comparison of the traditional MID measurements with data obtained with our method shows a good agreement, indicating the validity and feasibility of our

approach (Fig. 7).

Quantitative comparison of the same m/z is possible, but should be treated with extreme care. A proper reference is to be taken. Hence, we suspect that MID mode measurements and dedicated experiments with multiple cycles are better suited to this aim. The true merit of our method is that it quickly allows to scan a large number of masses for potentially interesting or unanticipated species, and get a broad overview of the gas mix in the reactor.

$HOAl(CH_3)_2$ has been detected before,[27] not in steady state, but during intial growth on a Si-H surface. It was shown with IR measurements and DFT calculations that the reaction of TMA with gas-phase water impurities may lead to this product. The formation of $HOAl(CH_3)_2$ then assisted in interlayer formation between Si-H and Al_2O_3. This study focused on $HOAl(CH_3)_2$ formation during the TMA pulse, where indeed OH is quickly captured from stray water molecules. In our case, it is detected during the water pulse, and as the TMA partial pressures drop below detection limit in between, the $Al(CH_3)_2$ group originates from the surface.

Atomistic modelling of surface reactions

Computational studies based on various surface models have all confirmed that CH_4 should be the dominant by-product on thermodynamic and kinetic grounds.[28–30] However, detecting $HOAl(CH_3)_2$ as a reaction product indicates competition of this mechanism with non-growth (etch) reactions, where Al and O are removed from the surface. It is clearly important to find out which reagent causes the non-growth reaction and whether particular surface intermediates or reactor conditions are involved. For the TMA-water system this means considering reactions of each of the two reagents on the possible surface-bound methylated fragments ($-Al(CH_3)_2$, $-Al(CH_3)$ and combinations thereof) and at a range of hydroxyl coverages ($-OH$). Hydroxyl coverage is known to decrease with temperature, but increasing temperature could also conceivably favor the larger by-product molecule via entropy, and so it is important to compare Gibbs free energies at the temperatures of interest.

Therefore, for each surface intermediate with a certain configuration of methyl and hydroxyl groups, we compare side-by-side the energetics of the potentially-competing growth and non-growth reactions with CH_4 and $HOAl(CH_3)_2$ as respective by-products. The reaction thermodynamics (ΔE at T=0 K and ΔG at T=25 °C and T=226.85 °C (500K)) for the competing reactions are computed, recognizing that the alternative by-product can only be formed from a particular surface intermediate if the non-growth reaction is exothermic.

Multiple reaction pathways for the formation of CH_4 and molecular $HOAl(CH_3)_2$ are considered at the created surfaces. We will describe these reaction pathways in the two pulses for a range of 11/8 monolayer of oxygen (MLO, see experimental section) to 9/8 MLO. Five and two reaction pathways are considered in the oxygen and the metal pulse, respectively (Table 1). These reaction pathways are depicted in the supplementary information. To describe the reaction pathways, the initial and the final optimized configurations with the highest OH-coverage of each reaction are depicted.

The surface-bound fragments $-Al(CH_3)$ and $-Al(CH_3)_2$ are the two main species that could remain from the interaction of the $Al(CH_3)_3$ molecule with the growing oxide surface in the metal pulse. The bidentate $-Al(CH_3)$ fragment is the energetically most favorable configuration in the metal pulse, since desorption of its last ligand is confronted with a large energetic barrier.[29] However, the monodentate $-Al(CH_3)_2$ fragment may also be present. Its formation is energetically favorable during the metal precursor pulse, as we will show below, and loss of further ligands from this fragment may not always occur, due to a lack of either H atoms or reactive O sites near the adsorbed fragment. In addition, the calculated activation energy shows a large barrier in the absence of the cooperative effect.[6] Hence, depending on the local chemistry at the surface, mono-and bidentate $-Al(CH_3)_x$ species will co-exist at the end of the metal precursor pulse.

Table 1: Reaction energy and Gibbs free energy of chemical reactions in ALD of Al_2O_3 by $Al(CH_3)_3/H_2O$ in steady state deposition mode.

Reaction	*Chemical formula of reactant slab*	*OH-coverage MLO*	*MLH*	ΔE (eV)	ΔG(eV) 25 °C	ΔG(eV) 226.85 °C
1.$Al(CH_3)(s) + H_2O(g) \longrightarrow AlOH(s) + CH_4(g)$	$Al_{33}O_{60}C_1H_{25}$	11/8	8/8	-1.14	-1.12	-1.04
	$Al_{33}O_{59}C_1H_{23}$	10/8	6/8	-1.03	-1.00	-0.93
	$Al_{33}O_{58}C_1H_{21}$	9/8	4/8	-1.10	-1.07	-1.00
2.$Al(CH_3)_2(s) + H_2O(g) \longrightarrow AlOH(CH_3)(s) + CH_4(g)$	$Al_{33}O_{60}C_2H_{29}$	11/8	9/8	-1.88	-1.85	-1.78
	$Al_{33}O_{59}C_2H_{27}$	10/8	7/8	-1.71	-1.69	-1.61
	$Al_{33}O_{58}C_2H_{25}$	9/8	5/8	-1.66	-1.64	-1.56
3.$Al(CH_3)_2(s) + O(s) + H_2O(g) \longrightarrow OH(s) + HOAl(CH_3)_2(g)$	$Al_{33}O_{60}C_2H_{29}$	11/8	9/8	0.57	0.34	0.24
	$Al_{33}O_{59}C_2H_{27}$	10/8	7/8	1.06	0.83	0.73
	$Al_{33}O_{58}C_2H_{25}$	9/8	5/8	1.64	1.31	1.41
4.$Al(CH_3)(s) + Al(CH_3)_2(s) + H_2O(g) \longrightarrow Al(s) + CH_4(g) + HOAl(CH_3)_2(g)$	$Al_{34}O_{60}C_3H_{30}$	11/8	7/8	-1.85	-2.65	-3.22
	$Al_{34}O_{59}C_3H_{28}$	10/8	5/8	-0.36	-1.16	-1.73
	$Al_{34}O_{58}C_3H_{26}$	9/8	3/8	1.73	0.94	0.36
5.$HOAl(CH_3)_2(s) \longrightarrow HOAl(CH_3)_2(g)$	$Al_{33}O_{59}C_2H_{27}$	11/8	9/8	2.52	1.70	1.05
	$Al_{33}O_{58}C_2H_{25}$	10/8	7/8	2.54	1.72	1.07
	$Al_{33}O_{57}C_2H_{23}$	9/8	5/8	3.05	2.22	1.58
6.$OH(s) + Al(CH_3)_3(g) \longrightarrow O(s) + Al(CH_3)_2(s) + CH_4(g)$	$Al_{33}O_{59}C_3H_{31}$	11/8	10/8	-1.82	-1.55	-1.37
	$Al_{33}O_{58}C_3H_{29}$	10/8	8/8	-1.60	-1.33	-1.14
	$Al_{33}O_{57}C_3H_{27}$	9/8	6/8	-3.58	-3.31	-3.13
7.$OH(s) + OH(s) + Al(CH_3)_3(g) \longrightarrow O(s) + HOAl(CH_3)_2(g) + CH_4(g)$	$Al_{33}O_{59}C_3H_{31}$	11/8	10/8	0.89	0.34	-0.11
	$Al_{33}O_{58}C_3H_{29}$	10/8	8/8	0.29	-0.25	-0.71
	$Al_{33}O_{57}C_3H_{27}$	9/8	6/8	0.31	-0.23	-0.69

Reactions in the water pulse

In this pulse, the H_2O molecule interacts with the remaining methyl groups at the Al_2O_3 surface. In the standard mechanistic picture of oxide ALD, dissociative adsorption of the H_2O molecule on these Al-CH_3 fragments leads to proton transfer, CH_4 formation and deposition of O as an OH group. The net replacement of a methyl group by a hydroxyl group is often termed ligand exchange, even though the mechanism can be more complex. (Fig. S5 and Fig. S6). These reactions are calculated for different OH-coverages and are evidently exothermic in all cases (Table 1, reactions 1 and 2). As a general trend, the reaction energy of methane formation from $-Al(CH_3)_2$ (average ΔE=-1.75 eV) is more favorable than that from $-Al(CH_3)$ (average ΔE=-1.09 eV), since the former occurs along with densification of the Al fragment to the oxide surface. The contributions of entropy to the Gibbs free energy of H_2O adsorption and CH_4 desorption are 0.59 eV and 0.56 eV per molecule at 25 °C and 1.14 eV and 1.04 eV per molecule at 226.85 °C, respectively. The net effect of inclusion of these entropic contributions is to make the reaction energy slightly positive, with entropy changes for H_2O adsorption and CH_4 desorption almost canceling each other out. Hence, in this reaction pathway, the entropic contribution is relatively small.

With CH_4 formation as an established exothermic baseline, we now consider different cases for the formation of $HOAl(CH_3)_2$. This molecule could be formed either from the dissociative adsorption of H_2O or directly from surface hydroxyl groups.

In the case of dissociative adorption, the hydroxyl ligand of $HOAl(CH_3)_2$ is provided from the dissociation of the H_2O molecule (Table 1, reaction 3). Al sites on the surface are not geometrically accessible to incoming H_2O. The H-atom of the H_2O molecule is transferred either to the neighboring oxygen or to the neighboring methyl group. The neighboring oxygen is coordinated to the Al of an $Al(CH_3)_2$ fragment that can participate in the dissociation of the H_2O molecule (Fig. S7). Reaction 3 is computed to be endothermic for different OH-coverages.

The entropic contribution of $HOAl(CH_3)_2$ desorption is 0.82 eV at 25 °C and 1.46 eV

per molecule at 226.85 °C. Hence, as expected, the extra degrees of freedom of the desorbing $HOAl(CH_3)_2$ molecule make this reaction more favorable with increasing temperature. However, the entropic effect is not sufficient to make reaction 3 exothermic overall at 226.85 °C.

In a previous study,[6] it was shown that a cooperative effect between neighboring $AlCH_3$ fragments facilitates dissociation of the H_2O co-reagent, ligand protonation, and subsequent ligand desorption. We therefore investigate whether the cooperative effect may help to explain $HOAl(CH_3)_2$ formation. To do this, we assume that the remaining $-Al(CH_3)_2$ and $-Al(CH_3)$ fragments are located beside each other and that they cooperate to dissociate an H_2O molecule (Fig. 9). H-transfer to the neighboring methyl group leads to CH_4 formation and OH-transfer to the $-Al(CH_3)_2$ leads to $HOAl(CH_3)_2$ formation. This reaction (Table 1, reaction 4) is exothermic by -1.85 eV and -0.36 eV at the OH-coverages of 11/8 MLO & 7/8 MLH and 10/8 MLO & 5/8 MLH, respectively. However, the reaction is endothermic by 1.73 eV at the OH-coverage of 9/8 MLO & 3/8 MLH. Lowering the OH coverage means that there are more basic O sites at the surface, which makes the desorption of molecules less favorable. The inclusion of entropy makes the reaction much more favorable at elevated temperature, as two desorbing by-product molecules are formed from one adsorbing reagent molecule.

We also consider the pathway for spontaneous desorption of the $HOAl(CH_3)_2$ molecule from the surface, without the action of any reagent. This can happen if the hydroxyl ligand of $HOAl(CH_3)_2$ is provided from the surface (Fig. S8). The calculations show that this reaction is entirely endothermic for the different OH-coverages (Table 1, reaction 5), even when entropy is included, indicating a substantial energy cost for breaking the bonds between molecule and surface.

Reactions 6 and 7 concern the TMA pulse and are treated in the supporting information, section .

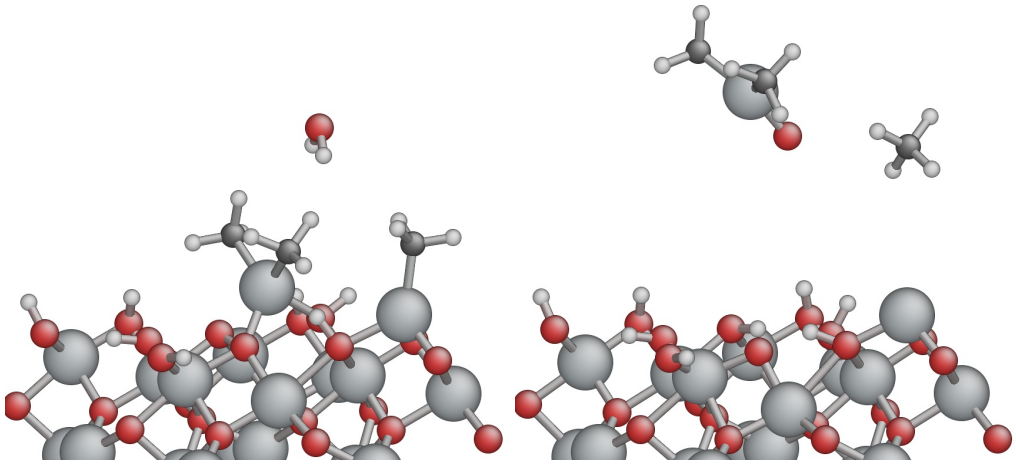

Figure 9: Graphical depiction of the dissociative adsorption of H_2O molecule onto $Al(CH_3)_2$ and $Al(CH_3)$ fragments (tab 1, reaction 4). The fragments cooperate to dissociate the H_2O molecule, leading to the desorption of both methane and molecular $HOAl(CH_3)_2$.

Discussion

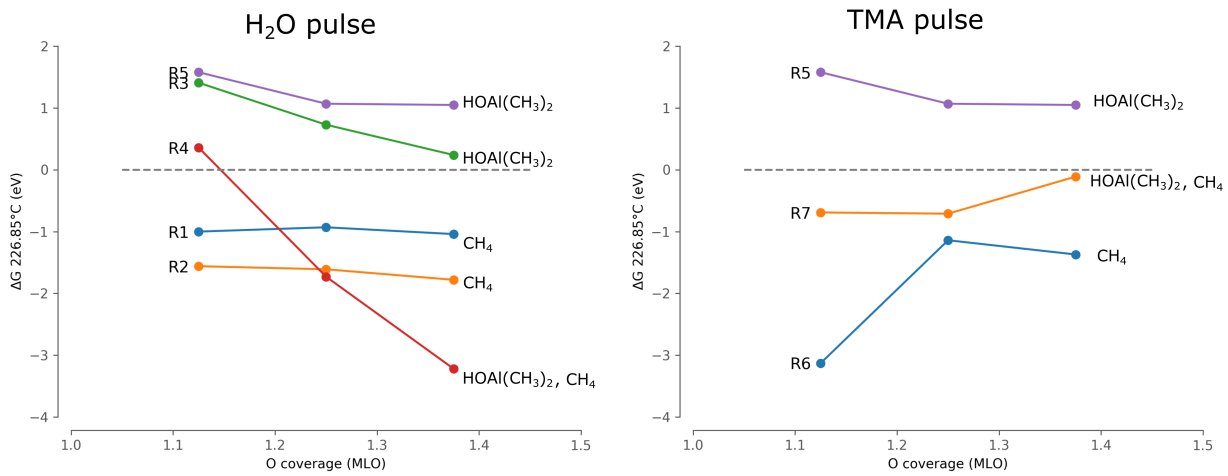

Figure 10: The calculated Gibbs free energy of chemical reactions in the oxygen pulse (left panel) and the metal pulse (right panel). Energy profiles are compiled from the energies in Table 1.

The detection and theoretical verification of an unknown reaction product for a process as ubiquitous as TMA-water perfectly illustrates the advantages of full-range *in situ* mass spectrometry over traditional approaches. As a complete image of the gas mix in the reactor during a full cycle is obtained with this method, and because it does not need dedicated

hardware and solely relies on post-processing, we hope that it can become widely adopted.

DFT calculations provided fundamental insight into the reaction energy and Gibbs free energy of chemical reactions in steady state deposition of Al_2O_3 from TMA-water. The Gibbs free energies of the chemical reactions in the oxygen pulse are depicted in the left panel of Fig. 10. For the chemical reactions in the metal precursor pulse they are depicted in the right panel of Fig. 10. Here, only ΔG at 226.85 °C is shown as a function of O-coverage. As the number of H atoms differs for each reaction pathway, the O-coverage is only shown.

The calculated free energies indicate that reactions 1 and 2 (leading to CH_4 formation) are generally the most energetically favorable reaction pathways when H_2O reacts with the surface and that methane is therefore the dominant by-product in this ALD pulse, as is also observed in Fig. 7. The calculated Gibbs free energy shows that the reactions are exothermic at all OH-coverages.

The calculated free energies of reaction 4 indicate that the $HOAl(CH_3)_2$ molecule may additionally be formed via a cooperative effect between multiple $Al{-}CH_3$ fragments. This becomes the energetically dominant pathway at high OH coverage, which can be expected towards the end of the H_2O pulse when the surface becomes saturated with OH groups. On the other hand, depletion of methyl groups towards the end of the H_2O pulse means less likelihood of the cooperative effect. Obviously, the complex pathway for reaction 4 may face substantial kinetic barriers; computing activation energies and inputting them into a micro-kinetic model, like atomistic kinetic Monte Carlo (KMC),[31] could provide a stronger insight into the competition between these reaction pathways.

The calculated Gibbs free energies indicate that both reactions 6 and 7 are thermodynamically viable when TMA adsorbs to any OH-covered surface. In reaction 7, along with CH_4 formation, molecular $HOAl(CH_3)_2$ can be formed and this is a potential route by which the $Al(CH_3)_3$ reagent can scavenge hydroxyl groups from the surface without contributing to deposition. However, reaction 6 is more strongly favored, particularly as OH-coverage decreases during the course of the metal pulse, which means that methane is likely to become

the exclusive by-product as the metal pulse proceeds.

Desorption of $HOAl(CH_3)_2$ has the effect of etching Al off the surface during the H_2O pulse, while during the TMA pulse it removes OH from the surface. Both result in a lower growth rate for ALD. However, only during the water pulse $HOAl(CH_3)_2$ was experimentally observed.

Etching side-reactions have been observed in ALD processes before.[32–36] However, the etching of Al during the water pulse in the TMA-water process is a curious phenomenon. While we do not yet have computed activation energies for this reaction, there might be very well a link with the temperature- and coverage-dependent saturation behavior suggested by Vandalon[37] and Sperling.[8] Sperling suggested a reaction probability of the form $S = B\exp(-(E+\beta\theta)/kT)$ for water, with B the reaction cross-section times the full-coverage surface density, $E + \beta\theta$ the effective, coverage (θ)-dependent activation energy, k the Boltzmann constant and T the temperature. Given our results, we can suggest a reaction rate of the form $S = A\exp(-E_0/kT) + B\exp(-(E_1 + \beta\theta)/kT)$, where the first term reflects the non-coverage dependent reactions with methane as a reaction product (reactions 1 and 2 from table 1) and the second term reflects the coverage dependent etching via $HOAl(CH_3)_2$. Dependent on the surface coverage and the temperature, one of the two terms can become dominant. Further analysis is certainly necessary here, but falls beyond the scope of this paper.

Conclusions

Applying a dedicated pulsing scheme and exploiting the cyclic nature of ALD allowed us to measure full m/z spectra in a time-resolved way, while only exposing the inside of the mass spectrometer to a single full ALD cycle. We were able to demonstrate that combining these spectra bypasses the limited time resolution of the mass spectrometer. The method presented here, based on post-processing, shows a way to keep track of all masses within the range of

interest and with a good time resolution. This was shown with data on the well-established TMA-water process. After confirming the generally accepted ligand exchange reaction, we found indications for $HOAl(CH_3)_2$ as a reaction product during the H_2O reaction. DFT calculations were performed, and it was shown that this reaction product can form and desorb from the surfaces at high OH-coverage towards the end of the water pulse, effectively etching the remaining Al from the surface. The reaction forming $HOAl(CH_3)_2$ depends on a cooperative effect between two adjacent surface groups, and becomes energetically more favorable than the formation of methane with increased OH-coverage. This is the first step towards computing activation energies and hence reaction kinetics for those particular intermediates in the future, and thus quantifying the relative amounts of the two by-products. In the TMA pulse, the formation of $HOAl(CH_3)_2$ as a reaction product is computed to be energetically possible as well, but less favorable than CH_4 formation, which remains the preferred mechanism. In the TMA pulse, $HOAl(CH_3)_2$ is not experimentally observed.

Supporting Information Available

The supporting information contains

- More details on the computational section.
- A video as an illustration of the noise minimization procedure.
- A section on the time resolution of the time-resolved full-range method
- A paragraph on on the signal at m/z 29.
- Figures of the reactions described in Table 1.
- A section on the formation of $HOAl(CH_3)_2$ in the metal pulse.
- Python functions used to process the data.

Acknowledgement

The authors acknowledge the financial support from the UGENT-GOA-01G01019 project. A.W. thanks the Fund for Scientific Research - Flanders (FWO) for a scholarship through an SB grant (number 1S12319N). J.D acknowledges the FWO for a post-doctoral fellowship (number 31527916). The computational work was carried out on the Compass computing cluster of the Department of Applied Physics at Eindhoven University of Technology. Hiden Analytical Ltd. is acknowledged for excellent technical support.

References

(1) Cremers, V.; Puurunen, R. L.; Dendooven, J. Conformality in atomic layer deposition: Current status overview of analysis and modelling. *Applied Physics Reviews* **2019**, *6*, 021302.

(2) Miikkulainen, V.; Leskelä, M.; Ritala, M.; Puurunen, R. L. Crystallinity of inorganic films grown by Atomic Layer Deposition: Overview and general trends. *Journal of Applied Physics* **2013**, *113*, 2.

(3) George, S. M. Atomic layer deposition: an overview. *Chemical Reviews* **2009**, *110*, 111–131.

(4) Puurunen, R. L. Surface chemistry of Atomic Layer Deposition: A case study for the trimethylaluminum/water process. *Journal of applied physics* **2005**, *97*, 9.

(5) Ylivaara, O. M.; Liu, X.; Kilpi, L.; Lyytinen, J.; Schneider, D.; Laitinen, M.; Julin, J.; Ali, S.; Sintonen, S.; Berdova, M. et al. Aluminum oxide from trimethylaluminum and water by atomic layer deposition: The temperature dependence of residual stress, elastic modulus, hardness and adhesion. *Thin Solid Films* **2014**, *552*, 124–135.

(6) Shirazi, M.; Elliott, S. D. Cooperation between adsorbates accounts for the activation of atomic layer deposition reactions. *Nanoscale* **2015**, *7*, 6311–6318.

(7) Guerra-Nuñez, C.; Döbeli, M.; Michler, J.; Utke, I. Reaction and growth mechanisms in Al_2O_3 deposited via atomic layer deposition: elucidating the hydrogen source. *Chemistry of Materials* **2017**, *29*, 8690–8703.

(8) Sperling, B. A.; Kalanyan, B.; Maslar, J. E. Atomic Layer Deposition of Al_2O_3 Using Trimethylaluminum and H_2O: The Kinetics of the H_2O Half-Cycle. *The Journal of Physical Chemistry C* **2020**, *124*, 3410–3420.

(9) Langereis, E.; Heil, S.; Knoops, H.; Keuning, W.; Van de Sanden, M.; Kessels, W. In situ spectroscopic ellipsometry as a versatile tool for studying atomic layer deposition. *Journal of Physics D: Applied Physics* **2009**, *42*, 73001.

(10) Rocklein, M.; George, S. Temperature-induced apparent mass changes observed during quartz crystal microbalance measurements of atomic layer deposition. *Analytical Chemistry* **2003**, *75*, 4975–4982.

(11) Chabal, Y. J. Surface infrared spectroscopy. *Surface Science Reports* **1988**, *8*, 211–357.

(12) Ritala, M.; Juppo, M.; Kukli, K.; Rahtu, A.; Leskelä, M. In situ characterization of atomic layer deposition processes by a mass spectrometer. *Le Journal de Physique IV* **1999**, *9*, Pr8–1021 – Pr8–1028.

(13) Devloo-Casier, K.; Ludwig, K. F.; Detavernier, C.; Dendooven, J. In situ synchrotron based x-ray techniques as monitoring tools for atomic layer deposition. *Journal of Vacuum Science & Technology A: Vacuum, Surfaces, and Films* **2014**, *32*, 010801.

(14) Knapas, K.; Ritala, M. In situ studies on reaction mechanisms in atomic layer deposition. *Critical reviews in solid state and materials sciences* **2013**, *38*, 167–202.

(15) George, S. M.; Lee, Y. Prospects for thermal atomic layer etching using sequential, self-limiting fluorination and ligand-exchange reactions. *ACS Nano* **2016**, *10*, 4889–4894.

(16) Biemann, K. Contributions of mass spectrometry to peptide and protein structure. *Biomedical & environmental mass spectrometry* **1988**, *16*, 99–111.

(17) Hoffman, E. d.; Stroobant, V. Mass spectrometry: principles and applications. *West Sussex: John Wiley & Sons, Bruxellas, Bélgica* **2007**, *1*, 85.

(18) Knoops, H.; Langereis, E.; Van de Sanden, M.; Kessels, W. Reaction mechanisms of atomic layer deposition of TaN_x from $Ta(NMe_2)_5$ precursor and H_2-based plasmas. *Journal of Vacuum Science & Technology A: Vacuum, Surfaces, and Films* **2012**, *30*, 01A101.

(19) Elam, J. W.; Martinson, A. B. F.; Pellin, M. J.; Hupp, J. T. Atomic Layer Deposition of In_2O_3 Using Cyclopentadienyl Indium: A New Synthetic Route to Transparent Conducting Oxide Films. *Chemistry of Materials* **2006**, *18*, 3571–3578.

(20) Gebhard, M.; Letourneau, S.; Mandia, D. J.; Choudhury, D.; Yanguas-Gil, A.; Mane, A.; Sattelberger, A. P.; Elam, J. W. Formation of unsaturated hydrocarbons and hydrogen: surface chemistry of methyltrioxorhenium (VII) in ALD of mixed-metal oxide structures comprising Re (III) units. *Chemistry of Materials* **2019**, *31*, 7821–7832.

(21) McLafferty, F. W. Mass spectrometric analysis. Molecular rearrangements. *Analytical Chemistry* **1959**, *31*, 82–87.

(22) Kresse, G.; Hafner, J. Ab initio molecular dynamics for liquid metals. *Phys. Rev. B* **1993**, *47*, 558–561.

(23) Larsen, A. H.; Mortensen, J. J.; Blomqvist, J.; Castelli, I. E.; Christensen, R.; Dułak, M.; Friis, J.; Groves, M. N.; Hammer, B.; Hargus, C. et al. The atomic sim-

ulation environment—a Python library for working with atoms. *Journal of Physics: Condensed Matter* **2017**, *29*, 273002.

(24) Sperling, B. A.; Kimes, W. A.; Maslar, J. E.; Chu, P. M. Time-resolved Fourier transform infrared spectroscopy of the gas phase during atomic layer deposition. *Journal of Vacuum Science & Technology A: Vacuum, Surfaces, and Films* **2010**, *28*, 613–621.

(25) Sperling, B. A.; Hoang, J.; Kimes, W. A.; Maslar, J. E. Time-resolved surface infrared spectroscopy during atomic layer deposition. *Applied spectroscopy* **2013**, *67*, 1003–1012.

(26) Lu, J.; Liu, B.; Greeley, J. P.; Feng, Z.; Libera, J. A.; Lei, Y.; Bedzyk, M. J.; Stair, P. C.; Elam, J. W. Porous Alumina Protective Coatings on Palladium Nanoparticles by Self-Poisoned Atomic Layer Deposition. *Chemistry of Materials* **2012**, *24*, 2047–2055.

(27) Halls, M. D.; Raghavachari, K.; Frank, M. M.; Chabal, Y. J. Atomic layer deposition of Al_2O_3 on H-passivated Si: $Al(CH_3)_2OH$ surface reactions with H/Si (100)- $2\times$ 1. *Physical Review B* **2003**, *68*, 161302.

(28) Widjaja, Y.; Musgrave, C. B. Quantum chemical study of the mechanism of aluminum oxide atomic layer deposition. *Applied Physics Letters* **2002**, *80*, 3304–3306.

(29) Elliott, S. D.; Greer, J. C. Simulating the atomic layer deposition of alumina from first principles. *J. Mater. Chem.* **2004**, *14*, 3246–3250.

(30) Weckman, T.; Laasonen, K. First principles study of the atomic layer deposition of alumina by TMA-H_2O process. *Phys. Chem. Chem. Phys.* **2015**, *17*, 17322–17334.

(31) Shirazi, M.; Elliott, S. D. Atomistic kinetic Monte Carlo study of atomic layer deposition derived from density functional theory. *Journal of Computational Chemistry* **2014**, *35*, 244–259.

(32) Elam, J.; Libera, J.; Pellin, M.; Stair, P. C. Spatially controlled atomic layer deposition in porous materials. *Applied Physics Letters* **2007**, *91*, 243105.

(33) Hinkle, C.; Sonnet, A.; Vogel, E.; McDonnell, S.; Hughes, G.; Milojevic, M.; Lee, B.; Aguirre-Tostado, F.; Choi, K.; Kim, H. et al. GaAs interfacial self-cleaning by atomic layer deposition. *Applied Physics Letters* **2008**, *92*, 071901.

(34) Milojevic, M.; Contreras-Guerrero, R.; Lopez-Lopez, M.; Kim, J.; Wallace, R. Characterization of the "clean-up" of the oxidized Ge (100) surface by atomic layer deposition. *Applied Physics Letters* **2009**, *95*, 212902.

(35) Devloo-Casier, K.; Geiregat, P.; Ludwig, K. F.; van Stiphout, K.; Vantomme, A.; Hens, Z.; Detavernier, C.; Dendooven, J. A case study of ALD encapsulation of quantum dots: Embedding supported CdSe/CdS/ZnS quantum dots in a ZnO matrix. *The Journal of Physical Chemistry C* **2016**, *120*, 18039–18045.

(36) Verstraete, R.; Rampelberg, G.; Rijckaert, H.; Van Driessche, I.; Coetsee, E.; Duvenhage, M.-M.; Smet, P. F.; Detavernier, C.; Swart, H.; Poelman, D. Stabilizing Fluoride Phosphors: Surface Modification by Atomic Layer Deposition. *Chemistry of Materials* **2019**, *31*, 7192–7202.

(37) Vandalon, V.; Kessels, W. M. M. E. Revisiting the growth mechanism of atomic layer deposition of Al_2O_3: A vibrational sum-frequency generation study. *Journal of Vacuum Science & Technology A* **2017**, *35*, 05C313.

Graphical TOC Entry